Topological derivative for the inverse scattering of elastic waves

B. B. Guzina, Marc Bonnet

TOPOLOGICAL DERIVATIVE FOR THE INVERSE SCATTERING OF ELASTIC WAVES

by B. B. GUZINA

(*Department of Civil Engineering, University of Minnesota, Minneapolis Minnesota 55455-0116, USA*)

M. BONNET

(*Laboratoire de Mécanique des Solides, École Polytechnique F-91128 Palaiseau Cedex, France*)

[Received 5 December 2002. Revise 20 May 2003]

Summary

To establish an alternative analytical framework for the elastic-wave imaging of underground cavities, the focus of this study is an extension of the concept of topological derivative, rooted in elastostatics and shape optimization, to three-dimensional elastodynamics involving semi-infinite and infinite solids. The main result of the proposed boundary integral approach is a formula for topological derivative, explicit in terms of the elastodynamic fundamental solution, obtained by an asymptotic expansion of the misfit-type cost functional with respect to the creation of an infinitesimal hole in an otherwise intact (semi-infinite or infinite) elastic medium. Valid for an arbitrary shape of the infinitesimal cavity, the formula involves the solution to six canonical exterior elastostatic problems, and becomes fully explicit when the vanishing cavity is spherical. A set of numerical results is included to illustrate the potential of topological derivative as a computationally efficient tool for exposing an approximate cavity topology, location, and shape via a grid-type exploration of the host solid. For a comprehensive solution to three-dimensional inverse scattering problems involving elastic waves, the proposed approach can be used most effectively as a pre-conditioning tool for more refined, albeit computationally intensive minimization-based imaging algorithms. To the authors' knowledge, an application of topological derivative to inverse scattering problems has not been attempted before; the methodology proposed in this paper could also be extended to acoustic problems.

1. Introduction

Stress-wave identification of cavities and objects embedded in an elastic solid is a long-standing problem in mechanics prompted by its applications in exploration seismology, nondestructive material testing, and underground facility detection. For this class of inverse scattering problems, often associated with the semi-infinite domain assumption for the 'host' elastic solid and free-surface distribution of motion sensors, a variety of approaches are available. Most of such imaging solutions are based either on the far-field approximation of the wave equation (ray theory, see (**1**)), or its finite-difference analogue (**2**). In order

to provide comprehensive three-dimensional subterranean images, however, these domain methods commonly necessitate an extensive experimental and computational effort.

For problems where rapid imaging of underground openings is required, on the other hand, the boundary integral equation (BIE) formulations, which furnish a direct mathematical link between the observed surface waveforms and the geometry of a hidden object, could be used to effectively compensate for the limited field data and expedite the interpretation process (see (**3**) for acoustic problems). In the context of elastic-wave imaging, however, an appreciable computational cost of the relevant half- or full-space fundamental solutions precludes the use of BIE methods in conjunction with global search techniques like genetic algorithms which entail a large number of forward simulations. As a result, an expedient BIE identification of subterranean cavities (or material defects) via elastic waves is amenable primarily in terms of the gradient-based optimization techniques, especially with the help of analytical shape sensitivity estimates (**4**). Unfortunately, the stand-alone use of gradient-type minimization for such purpose is not satisfactory for its success is strongly dependent on a reliable prior information about the geometry of the hidden void.

These considerations led the authors to investigate the usefulness of the concept of *topological derivative* in connection with the elastodynamic inverse problem. Considering a generic cost functional $\mathcal{J}$ of the void shape, size, location, and topology, its topological derivative, $\mathcal{T}(\boldsymbol{x}^0)$, synthesizes the sensitivity of $\mathcal{J}$ with respect to the creation of an infinitesimal cavity at a prescribed location $\boldsymbol{x}^0$ inside the host solid. The information provided by the topological derivative distribution $\mathcal{T}(\boldsymbol{x}^0)$ is thus potentially very useful, providing a rational basis for selecting the void topology and its initial location/geometry, both of which are necessary for the application of gradient-based minimization to the inverse scattering problem at hand. The concept of topological derivative first appeared in (**5**) and (**6**) in the context of shape optimization of mechanical structures. Recently, its rigorous mathematical formulation has been established within the framework of elastostatic problems and Laplace equation (**7**, **8**). Beyond its direct application to the structural shape optimization problems, however, the topological derivative may also have potential use in solving inverse problems, a topic in its early stages of investigation to which the present article is intended to contribute (see also (**9**) for two-dimensional elastostatics).

In this communication, the concept of topological derivative is extended to three-dimensional inverse scattering of elastic waves involving semi-infinite and infinite domains. In the approach, the formula for topological derivative (explicit in terms of the fundamental solution) is obtained within the framework of BIE methods by an asymptotic expansion of the featured cost functional with respect to the creation of an infinitesimal hole in the intact host solid. Dependent on the prescribed shape of the infinitesimal cavity, the formula involves the solution to six exterior elastostatic problems, and becomes fully explicit if the infinitesimal cavity is spherical. A set of numerical results is included to illustrate the approach, which could be used most effectively as a pre-conditioning tool for more accurate gradient-based imaging algorithms (**4**). Reliant on the availability of suitable fundamental solutions, the proposed method could be directly extended to elastic-wave imaging of finite solid bodies.

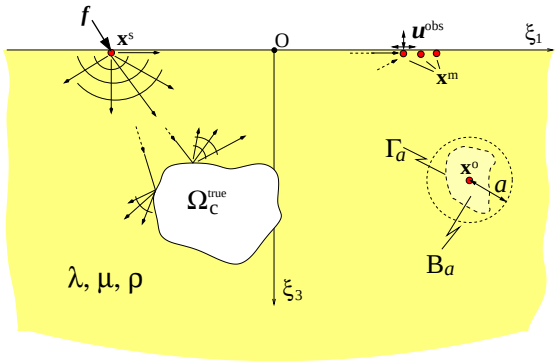

Fig. 1 Illumination of an underground cavity ($\Omega_{\rm C}^{\rm true}$) by elastic waves

2. Inverse problem

Consider the imaging problem depicted in Fig. 1 where the semi-infinite solid, probed by elastic waves, houses a hidden void (or a system thereof). With the Cartesian frame $\{O:\xi_1,\xi_2,\xi_3\}$ set at the top surface S, the homogeneous isotropic half-space $\Omega=\{(\xi_1,\xi_2,\xi_3)|\xi_3>0\}$ is characterized by the Lamé constants λ and μ, and mass density ρ. Without loss of generality, it will be assumed that the sought cavity, $\Omega_{\rm C}^{\rm true}\subset\Omega$, is illuminated by a time-harmonic point source $\boldsymbol{f}$ acting at $\boldsymbol{\xi}=\boldsymbol{x}^{\rm s}\in\Omega$ with frequency ω. For imaging purposes, the induced surface motion $\boldsymbol{u}^{\rm obs}$ is monitored over a finite set of control points $\boldsymbol{\xi}=\boldsymbol{x}^m\in\Omega$ $(m=1,2,\dots M)$.

Following the conventional approach (**4**), the cost function for the inverse scattering problem described in Fig. 1 can be defined in a misfit-type fashion as

$$\mathcal{J}(\Omega\backslash\overline{\Omega}_{\rm C};\boldsymbol{f})=\frac{1}{2}\sum_{m=1}^{M}\{\overline{\boldsymbol{u}(\boldsymbol{x}^m,\omega)-\boldsymbol{u}^{\rm obs}(\boldsymbol{x}^m,\omega)}\}\cdot\boldsymbol{W}^m\cdot\{\boldsymbol{u}(\boldsymbol{x}^m,\omega)-\boldsymbol{u}^{\rm obs}(\boldsymbol{x}^m,\omega)\},\qquad(2.1)$$

where $\overline{\Omega}_{\rm C}=\Omega_{\rm C}\cup\Gamma$ indicates the closure of a *trial* cavity $\Omega_{\rm C}$ bounded by a closed smooth surface Γ; over-bar symbol denotes complex conjugation; $\boldsymbol{W}^m$ $(m=1,2,\dots,M)$ are suitable Hermitian and positive definite matrices, and $\boldsymbol{u}$ is the displacement field which solves the elastodynamic scattering problem for the semi-infinite solid $\Omega\backslash\overline{\Omega}_{\rm C}$: $\boldsymbol{u}$ satisfies the field equations

$$\nabla\cdot(\boldsymbol{C}:\nabla\boldsymbol{u})+\boldsymbol{f}=-\rho\,\omega^2\boldsymbol{u},\qquad\boldsymbol{\xi}\in\Omega\setminus\overline{\Omega}_{\rm C},\qquad(2.2)$$

and Neumann boundary conditions

$$\boldsymbol{t}\equiv\boldsymbol{n}\cdot\boldsymbol{C}:\nabla\boldsymbol{u}=\boldsymbol{0},\qquad\boldsymbol{\xi}\in\Gamma\cup S.\qquad(2.3)$$

Here, $\boldsymbol{t}$ denotes the surface traction, $\boldsymbol{n}$ is the unit normal on Γ outward to $\Omega\backslash\overline{\Omega}_{\rm C}$, and

$$\boldsymbol{C}=\lambda\,\mathbf{I}_2\otimes\mathbf{I}_2+2\mu\,\mathbf{I}_4^{\rm sym}\qquad(2.4)$$

is the isotropic elasticity tensor with $\mathbf{I}_2$ and $\mathbf{I}_4^{\rm sym}$ symbolizing the second-order and symmetric fourth-order identity tensors, respectively.

In what follows, it is assumed that $\boldsymbol{u}$ satisfies the standard continuity requirements for smooth bounding surfaces, $\boldsymbol{u}\in C^2(\Omega\setminus\overline{\Omega_{\rm C}})\cap C^1((\Omega\setminus\Omega_{\rm C})\cup S)$. For this class of scattering problems, the displacement field $\boldsymbol{u}$ satisfying (2.2) and (2.3) can be shown to admit a Somigliana-type integral representation (**10**)

$$\boldsymbol{u}(\boldsymbol{x},\omega)=\boldsymbol{e}_k\int_\Gamma \boldsymbol{t}(\boldsymbol{\xi},\omega;\boldsymbol{n})\cdot\hat{\boldsymbol{u}}^k(\boldsymbol{\xi},\boldsymbol{x},\omega)\,\mathrm{d}\Gamma_\xi \;-\; \boldsymbol{e}_k\int_\Gamma \boldsymbol{u}(\boldsymbol{\xi},\omega)\cdot\hat{\boldsymbol{t}}^k(\boldsymbol{\xi},\boldsymbol{x},\omega;\boldsymbol{n})\,\mathrm{d}\Gamma_\xi + \;\boldsymbol{e}_k\int_{\Omega\setminus\overline{\Omega}_{\rm C}}\boldsymbol{f}(\boldsymbol{\xi},\omega)\cdot\hat{\boldsymbol{u}}^k(\boldsymbol{\xi},\boldsymbol{x},\omega)\,\mathrm{d}\Omega_\xi,\qquad \boldsymbol{x}\in\Omega\setminus\overline{\Omega}_{\rm C},\quad (2.5)$$

where $\boldsymbol{e}_k$ is the unit vector in the ξ_k-direction ($k=1,2,3$); Einstein summation convention is assumed over the spatial coordinate index k, and $\hat{\boldsymbol{u}}^k(\boldsymbol{\xi},\boldsymbol{x},\omega)$ and $\hat{\boldsymbol{t}}^k(\boldsymbol{\xi},\boldsymbol{x},\omega;\boldsymbol{n})$ constitute the elastodynamic fundamental solution for a uniform *semi-infinite* solid by denoting the respective displacement and traction vectors at $\boldsymbol{\xi}\in\Omega$ due to a unit (time-harmonic) point force acting at $\boldsymbol{x}\in\Omega$ in the kth direction. As shown in (**11**), these Green's functions can be decomposed into a singular part $([\hat{\boldsymbol{u}}]_1,[\hat{\boldsymbol{t}}]_1)$ and a residual (regular) component $([\hat{\boldsymbol{u}}]_2,[\hat{\boldsymbol{t}}]_2)$ via

$$\begin{aligned}\hat{u}_i^k(\boldsymbol{\xi},\boldsymbol{x},\omega)&=[\hat{u}_i^k(\boldsymbol{\xi},\boldsymbol{x},\omega)]_1\;+\;[\hat{u}_i^k(\boldsymbol{\xi},\boldsymbol{x},\omega)]_2,\\ \hat{t}_i^k(\boldsymbol{\xi},\boldsymbol{x},\omega;\boldsymbol{n})&=[\hat{t}_i^k(\boldsymbol{\xi},\boldsymbol{x},\omega;\boldsymbol{n})]_1\;+\;[\hat{t}_i^k(\boldsymbol{\xi},\boldsymbol{x},\omega;\boldsymbol{n})]_2,\end{aligned}\qquad (2.6)$$

where, for point forces located at a non-zero distance from the free surface ($x_3>0$), $[\hat{\boldsymbol{u}}]_1$ and $[\hat{\boldsymbol{t}}]_1$ are given by the (elastostatic) Kelvin solution for an infinite solid.

For the ensuing treatment, the total displacement field $\boldsymbol{u}$ featured in (2.5) can be conveniently decomposed as

$$\boldsymbol{u}(\boldsymbol{\xi},\omega)=\boldsymbol{u}^{\rm F}(\boldsymbol{\xi},\omega)+\boldsymbol{u}^{\rm S}(\boldsymbol{\xi},\omega),\qquad \boldsymbol{\xi}\in\Omega\setminus\overline{\Omega}_{\rm C},\qquad (2.7)$$

where $\boldsymbol{u}^{\rm S}$ denotes the *scattered field*, and $\boldsymbol{u}^{\rm F}$ is the free (incident) field defined as the response of a cavity-free half-space Ω due to given body force distribution $\boldsymbol{f}$. On the basis of the traction-free boundary condition (2.3) and the Maxwell-type symmetry of the fundamental solution where $\hat{u}_i^k(\boldsymbol{\xi},\boldsymbol{x},\omega)=\hat{u}_k^i(\boldsymbol{x},\boldsymbol{\xi},\omega)$, the first and the third term on the right-hand side of (2.5) reduce respectively to zero and $\boldsymbol{u}^{\rm F}$, resulting in an integral representation for the scattered field in the form of

$$\boldsymbol{u}^{\rm S}(\boldsymbol{x},\omega)=-\boldsymbol{e}_k\int_\Gamma \boldsymbol{u}(\boldsymbol{\xi},\omega)\cdot\hat{\boldsymbol{t}}^k(\boldsymbol{\xi},\boldsymbol{x},\omega;\boldsymbol{n})\,\mathrm{d}\Gamma_\xi,\qquad \boldsymbol{x}\in\Omega\setminus\overline{\Omega}_{\rm C}.\qquad (2.8)$$

3. Topological derivative

To search the semi-infinite domain Ω for cavities in the context of (2.1), let $B_a(\boldsymbol{x}^{\rm O})=\boldsymbol{x}^{\rm O}+a\mathcal{B}$ define the cavity of size $a>0$ and volume $a^3\,|\mathcal{B}|$, where $\mathcal{B}\subset\mathbb{R}^3$ is a *fixed* and bounded open set of volume $|\mathcal{B}|$ containing the origin. For further reference, B_a is assumed to be bounded by a simply connected, smooth surface Γ_a, with $\overline{B}_a=B_a\cup\Gamma_a$ denoting its closure. Without loss of generality, $\mathcal{B}$ is chosen so that $B_a(\boldsymbol{x}^{\rm O})$ is contained inside the sphere of radius a centred at $\boldsymbol{x}^{\rm O}$ (see Fig. 1). With such definitions, the topological derivative of (2.1) can be defined as

$$\mathcal{T}(\boldsymbol{x}^{\rm O},\boldsymbol{f})=\lim_{a\to0}\frac{\mathcal{J}(\Omega\setminus\overline{B}_a;\boldsymbol{f})-\mathcal{J}(\Omega;\boldsymbol{f})}{|B_a|}=\lim_{a\to0}\frac{\mathcal{J}(\Omega\setminus\overline{B}_a;\boldsymbol{f})-\mathcal{J}(\Omega;\boldsymbol{f})}{a^3\,|\mathcal{B}|},\quad \boldsymbol{x}^{\rm O}\in B_a,\quad (3.1)$$

which furnishes the information about the variation of $\mathcal{J}(\Omega;\boldsymbol{f})$ if a hole of prescribed shape $\mathcal{B}$ and infinitesimal characteristic size is created at $\boldsymbol{x}^{\mathrm{O}}\in\Omega$. Within the framework of shape optimization, it was shown (**7**, **8**) that the elastostatic equivalent of (3.1) can be used as a powerful tool for the grid-based exploration of a solid for plausible void regions in terms of the chosen shape functional $\mathcal{J}$. In what follows, this concept will be extended to elastic-wave imaging of semi-infinite solids on the basis of the elastodynamic fundamental solution for a homogeneous isotropic half-space. As pointed out earlier, the topological derivative is investigated here as a pre-conditioning tool for selecting the *initial* 'guess' for an optimization-based approach to the solution of inverse scattering problems, and is therefore considered *only* in relation to the unperturbed half-space Ω, as suggested by (3.1). The reader is referred to the end of Section 5 for further discussion on this subject.

4. Small cavity approximation

In the context of (3.1), the trial cavity featured in (2.5) to (2.8) can be specialized to a small void of size a containing $\boldsymbol{x}^{\mathrm{O}}$ so that $\Omega_{\mathrm{C}}=B_a(\boldsymbol{x}^{\mathrm{O}})$. For this problem, integral representation (2.8) can be conveniently expanded by virtue of (2.7) as

$$\boldsymbol{u}^{\mathrm{S}}(\boldsymbol{x},\omega)=\underbrace{-\boldsymbol{e}_k\int_{\Gamma_a}\boldsymbol{u}^{\mathrm{F}}(\boldsymbol{\xi},\omega)\cdot\hat{\boldsymbol{t}}^{k}(\boldsymbol{\xi},\boldsymbol{x},\omega;\boldsymbol{n})\,\mathrm{d}\Gamma_\xi}_{\boldsymbol{u}^{\mathrm{S,F}}}\ \underbrace{-\boldsymbol{e}_k\int_{\Gamma_a}\boldsymbol{u}^{\mathrm{S}}(\boldsymbol{\xi},\omega)\cdot\hat{\boldsymbol{t}}^{k}(\boldsymbol{\xi},\boldsymbol{x},\omega;\boldsymbol{n})\,\mathrm{d}\Gamma_\xi}_{\boldsymbol{u}^{\mathrm{S,S}}},\quad(4.1)$$

for $\boldsymbol{x}\in\Omega\backslash\overline{B}_a$, where $\boldsymbol{n}$ denotes the unit normal on Γ_a outward to the exterior domain. By means of the divergence theorem, the first term can be rewritten as

$$\begin{aligned}\boldsymbol{u}^{\mathrm{S,F}}(\boldsymbol{x},\omega)&=-\boldsymbol{e}_k\int_{\Gamma_a}\boldsymbol{n}(\boldsymbol{\xi})\cdot\hat{\boldsymbol{\sigma}}^{k}(\boldsymbol{\xi},\boldsymbol{x},\omega)\cdot\boldsymbol{u}^{\mathrm{F}}(\boldsymbol{\xi},\omega)\,\mathrm{d}\Gamma_\xi\\&=\boldsymbol{e}_k\int_{B_a}\Big\{\Big(\nabla_\xi\cdot\hat{\boldsymbol{\sigma}}^{k}(\boldsymbol{\xi},\boldsymbol{x},\omega)\Big)\cdot\boldsymbol{u}^{\mathrm{F}}(\boldsymbol{\xi},\omega)+\hat{\boldsymbol{\sigma}}^{k}(\boldsymbol{\xi},\boldsymbol{x},\omega):\nabla\boldsymbol{u}^{\mathrm{F}}(\boldsymbol{\xi},\omega)\Big\}\,\mathrm{d}\Omega_\xi,\end{aligned}\quad(4.2)$$

for $\boldsymbol{x}\in\Omega\backslash\overline{B}_a$, where $\hat{\boldsymbol{\sigma}}^{k}=(\hat{\boldsymbol{\sigma}}^{k})^{T}$ denotes the elastodynamic stress Green's function,

$$\nabla_\xi\cdot\hat{\boldsymbol{\sigma}}^{k}(\boldsymbol{\xi},\boldsymbol{x},\omega)+\delta(\boldsymbol{\xi}-\boldsymbol{x})\boldsymbol{e}_k=-\rho\omega^2\hat{\boldsymbol{u}}^{k}(\boldsymbol{\xi},\boldsymbol{x},\omega),\quad\boldsymbol{x},\boldsymbol{\xi}\in\Omega,\quad k=1,2,3.\quad(4.3)$$

To evaluate the limiting form of (4.2) as the cavity size a vanishes, one may invoke the Taylor expansion of $\hat{\boldsymbol{u}}^{k}$ inside the void,

$$\begin{aligned}\hat{\boldsymbol{u}}^{k}(\boldsymbol{\xi},\boldsymbol{x},\omega)&=\hat{\boldsymbol{u}}^{k}(\boldsymbol{x}^{\mathrm{O}},\boldsymbol{x},\omega)+(\boldsymbol{\xi}-\boldsymbol{x}^{\mathrm{O}})\cdot\nabla_\xi\hat{\boldsymbol{u}}^{k}(\boldsymbol{\xi},\boldsymbol{x},\omega)|_{\boldsymbol{\xi}=\boldsymbol{x}^{\mathrm{O}}}+\ldots,\\&\equiv\hat{\boldsymbol{u}}^{k}(\boldsymbol{x}^{\mathrm{O}},\boldsymbol{x},\omega)+\boldsymbol{\psi}(\boldsymbol{\xi},\boldsymbol{x}^{\mathrm{O}},\boldsymbol{x},\omega),\qquad\boldsymbol{\xi}\in B_a,\quad|\boldsymbol{\psi}|=O(a),\quad a\to0,\end{aligned}\quad(4.4)$$

and write similar expressions for $\hat{\boldsymbol{\sigma}}^{k}$, $\boldsymbol{u}^{\mathrm{F}}$, and $\nabla\boldsymbol{u}^{\mathrm{F}}$. As a result, on employing (4.3), the limiting behaviour of (4.2) as $a\to0$ can be reduced to

$$\begin{aligned}\boldsymbol{u}^{\mathrm{S,F}}&=a^3|\mathcal{B}|\;\boldsymbol{e}_k\Big\{\hat{\boldsymbol{\sigma}}^{k}(\boldsymbol{x}^{\mathrm{O}},\boldsymbol{x},\omega):\nabla\boldsymbol{u}^{\mathrm{F}}(\boldsymbol{\xi},\omega)|_{\boldsymbol{\xi}=\boldsymbol{x}^{\mathrm{O}}}-\rho\omega^2\hat{\boldsymbol{u}}^{k}(\boldsymbol{x}^{\mathrm{O}},\boldsymbol{x},\omega)\cdot\boldsymbol{u}^{\mathrm{F}}(\boldsymbol{x}^{\mathrm{O}},\omega)\Big\}+\boldsymbol{\eta}\\&=a^3|\mathcal{B}|\;\boldsymbol{e}_k\Big\{\frac{1}{2\mu}\,\hat{\boldsymbol{\sigma}}^{k}(\boldsymbol{x}^{\mathrm{O}},\boldsymbol{x},\omega):\boldsymbol{\sigma}^{\mathrm{F}}(\boldsymbol{x}^{\mathrm{O}},\omega)-\frac{\nu}{2\mu(1+\nu)}\,(\mathrm{tr}\,\hat{\boldsymbol{\sigma}}^{k}(\boldsymbol{x}^{\mathrm{O}},\boldsymbol{x},\omega))\,(\mathrm{tr}\,\boldsymbol{\sigma}^{\mathrm{F}}(\boldsymbol{x}^{\mathrm{O}},\omega))\\&\qquad-\rho\,\omega^2\hat{\boldsymbol{u}}^{k}(\boldsymbol{x}^{\mathrm{O}},\boldsymbol{x},\omega)\cdot\boldsymbol{u}^{\mathrm{F}}(\boldsymbol{x}^{\mathrm{O}},\omega)\Big\}\;+\;\boldsymbol{\eta}(\boldsymbol{x}^{\mathrm{O}},\boldsymbol{x},\omega),\quad\boldsymbol{x}\in\Omega\backslash\overline{B}_a,\end{aligned}\quad(4.5)$$

where $|\boldsymbol{\eta}| = o(a^3)$ as $a \to 0$, $\boldsymbol{\sigma}^{\mathrm{F}} = \frac{1}{2}\boldsymbol{C} : (\nabla \boldsymbol{u}^{\mathrm{F}} + \nabla^T \boldsymbol{u}^{\mathrm{F}})$ is the free-field stress tensor and $\nu = \lambda/\{2(\lambda+\mu)\}$ denotes the Poisson's ratio of the semi-infinite solid. It should be noted that (4.5) rests on the implicit assumption that $\boldsymbol{x}^{\mathrm{O}} \neq \boldsymbol{x}$, a hypothesis that will be addressed in the sequel.

4.1 *Boundary distribution of the scattered field*

To elucidate the contribution of the second term $\boldsymbol{u}^{\mathrm{S,S}}$ in (4.1) for diminishing a, it is necessary first to determine the asymptotic behaviour of the scattered field, $\boldsymbol{u}^{\mathrm{S}}$, along Γ_a in the limit as $a \to 0$. For the latter problem, one has

$$\begin{aligned} \nabla\cdot(\boldsymbol{C}:\nabla \boldsymbol{u}^{\mathrm{S}}) = -\rho\,\omega^2 \boldsymbol{u}^{\mathrm{S}}, \quad \boldsymbol{\xi} \in \Omega \setminus \overline{B}_a, \\ \boldsymbol{t}^{\mathrm{S}} = -\boldsymbol{t}^{\mathrm{F}} \quad \text{for } \boldsymbol{\xi} \in \Gamma_a \quad \text{and} \quad \boldsymbol{t}^{\mathrm{S}} = \boldsymbol{0} \quad \text{for } \boldsymbol{\xi} \in S, \end{aligned} \tag{4.6}$$

where $\boldsymbol{t}^{\mathrm{S}}$ and $\boldsymbol{t}^{\mathrm{F}}$ are the surface tractions associated respectively with $\boldsymbol{u}^{\mathrm{S}}$ and $\boldsymbol{u}^{\mathrm{F}}$. On the basis of (4.6), the regularized BIE for the scattered field (**10**) can be written as

$$\begin{aligned} \int_{\Gamma_a} \boldsymbol{t}^{\mathrm{F}}(\boldsymbol{\xi},\omega;\boldsymbol{n})\cdot\hat{\boldsymbol{u}}^k(\boldsymbol{\xi},\boldsymbol{x},\omega)\,\mathrm{d}\Gamma_\xi + \int_{\Gamma_a} (\boldsymbol{u}^{\mathrm{S}}(\boldsymbol{\xi},\omega) - \boldsymbol{u}^{\mathrm{S}}(\boldsymbol{x},\omega))\cdot[\hat{\boldsymbol{t}}^k(\boldsymbol{\xi},\boldsymbol{x},\omega;\boldsymbol{n})]_1\,\mathrm{d}\Gamma_\xi \\ + \int_{\Gamma_a} \boldsymbol{u}^{\mathrm{S}}(\boldsymbol{\xi},\omega)\cdot[\hat{\boldsymbol{t}}^k(\boldsymbol{\xi},\boldsymbol{x},\omega;\boldsymbol{n})]_2\,\mathrm{d}\Gamma_\xi = -u_k^{\mathrm{S}}(\boldsymbol{x},\omega), \quad \boldsymbol{x} \in \Gamma_a, \quad k = 1,2,3. \end{aligned} \tag{4.7}$$

For the ensuing developments, it is useful to employ (2.6) and rewrite (4.7) as

$$\begin{aligned} \int_{\Gamma_a} \boldsymbol{t}^{\mathrm{F}}(\boldsymbol{\xi},\omega;\boldsymbol{n})\cdot\Big([\hat{\boldsymbol{u}}^k(\boldsymbol{\xi},\boldsymbol{x},\omega)]_1 + [\hat{\boldsymbol{u}}^k(\boldsymbol{\xi},\boldsymbol{x},\omega)]_2\Big)\,\mathrm{d}\Gamma_\xi \\ + \int_{\Gamma_a} (\boldsymbol{u}^{\mathrm{S}}(\boldsymbol{\xi},\omega) - \boldsymbol{u}^{\mathrm{S}}(\boldsymbol{x},\omega))\cdot\Big([\hat{\boldsymbol{t}}^k(\boldsymbol{\xi},\boldsymbol{x},\omega;\boldsymbol{n})]_1 + [\hat{\boldsymbol{t}}^k(\boldsymbol{\xi},\boldsymbol{x},\omega;\boldsymbol{n})]_2\Big)\,\mathrm{d}\Gamma_\xi \\ = -\boldsymbol{u}^{\mathrm{S}}(\boldsymbol{x},\omega)\cdot\left(\boldsymbol{e}_k + \int_{\Gamma_a} [\hat{\boldsymbol{t}}^k(\boldsymbol{\xi},\boldsymbol{x},\omega;\boldsymbol{n})]_2\,\mathrm{d}\Gamma_\xi\right), \quad \boldsymbol{x} \in \Gamma_a, \quad k = 1,2,3. \end{aligned} \tag{4.8}$$

Under the assumption that the sampling point $\boldsymbol{x}^{\mathrm{O}}$ is located at a *fixed* non-zero (but otherwise arbitrary) depth inside the half-space, $[\hat{\boldsymbol{u}}]_1$ and $[\hat{\boldsymbol{t}}]_1$ in (4.8) are, for any sufficiently small a, given by the Kelvin's solution so that

$$\begin{aligned} &[\hat{\boldsymbol{u}}^k(\boldsymbol{\xi},\boldsymbol{x},\omega)]_1 = O\big(|\boldsymbol{\xi}-\boldsymbol{x}|^{-1}\big), \quad [\hat{\boldsymbol{u}}^k(\boldsymbol{\xi},\boldsymbol{x},\omega)]_2 = O(1) \\ &[\hat{\boldsymbol{t}}^k(\boldsymbol{\xi},\boldsymbol{x},\omega)]_1 = O\big(|\boldsymbol{\xi}-\boldsymbol{x}|^{-2}\big), \quad [\hat{\boldsymbol{t}}^k(\boldsymbol{\xi},\boldsymbol{x},\omega)]_2 = O(1), \quad \boldsymbol{\xi},\boldsymbol{x} \in \Gamma_a \Rightarrow |\boldsymbol{\xi}-\boldsymbol{x}| \leq 2a, \end{aligned} \tag{4.9}$$

as $a \to 0$. On utilizing (4.9) together with the expansion of the free-field traction

$$\begin{aligned} \boldsymbol{t}^{\mathrm{F}}(\boldsymbol{\xi},\omega) &= \boldsymbol{n}(\xi)\cdot\big\{\boldsymbol{\sigma}^{\mathrm{F}}(\boldsymbol{x}^{\mathrm{O}},\omega) + (\boldsymbol{\xi}-\boldsymbol{x}^{\mathrm{O}})\cdot\nabla\boldsymbol{\sigma}^{\mathrm{F}}(\boldsymbol{\xi},\omega)|_{\boldsymbol{\xi}=\boldsymbol{x}^{\mathrm{O}}} + \ldots\big\}, \\ &\equiv \boldsymbol{n}(\boldsymbol{\xi})\cdot\boldsymbol{\sigma}^{\mathrm{F}}(\boldsymbol{x}^{\mathrm{O}},\omega) + \boldsymbol{\phi}(\boldsymbol{\xi},\boldsymbol{x}^{\mathrm{O}},\omega), \quad |\boldsymbol{\phi}| = O(a), \quad \boldsymbol{\xi}\in\Gamma_a, \quad a \to 0, \end{aligned} \tag{4.10}$$

around $\boldsymbol{\xi}=\boldsymbol{x}^{\mathrm{O}}$, the limiting form of (4.8) as $a \to 0$ can be reduced to

$$\begin{aligned} \int_{\Gamma_a} \boldsymbol{n}(\boldsymbol{\xi})\cdot\boldsymbol{\sigma}^{\mathrm{F}}(\boldsymbol{x}^{\mathrm{O}},\omega)\cdot[\hat{\boldsymbol{u}}^k(\boldsymbol{\xi},\boldsymbol{x},\omega)]_1\,\mathrm{d}\Gamma_\xi + \int_{\Gamma_a} (\boldsymbol{v}(\boldsymbol{\xi},\omega) - \boldsymbol{v}(\boldsymbol{x},\omega))\cdot[\hat{\boldsymbol{t}}^k(\boldsymbol{\xi},\boldsymbol{x},\omega;\boldsymbol{n})]_1\,\mathrm{d}\Gamma_\xi \\ = -v_k(\boldsymbol{x},\omega), \qquad \boldsymbol{x} \in \Gamma_a, \quad k = 1,2,3, \end{aligned} \tag{4.11}$$

where $\boldsymbol{v}$ denotes the *leading* asymptotic behaviour of $\boldsymbol{u}^{\mathrm{S}}$ along the cavity boundary,

$$\boldsymbol{v}(\boldsymbol{\xi},\omega) = \operatorname*{Asym}_{a\to 0} \boldsymbol{u}^{\mathrm{S}}(\boldsymbol{\xi},\omega), \qquad \boldsymbol{\xi}\in\Gamma_a. \tag{4.12}$$

With reference to (2.6) and (4.6), a comparison of (4.7) and (4.11) reveals that $\boldsymbol{v}$ can be interpreted as an *elastostatic* solution of the exterior problem

$$\begin{aligned} \nabla\cdot(\boldsymbol{C}:\nabla\boldsymbol{v}) &= \boldsymbol{0}, && \boldsymbol{\xi}\in\mathbb{R}^3\setminus\overline{B}_a,\\ \boldsymbol{t}^v &= -\boldsymbol{n}\cdot\boldsymbol{\sigma}^{\mathrm{F}}(\boldsymbol{x}^{\mathrm{O}},\omega), && \boldsymbol{\xi}\in\Gamma_a, \end{aligned} \tag{4.13}$$

for the cavity B_a in an *infinite* elastic medium, where $\boldsymbol{t}^v = \boldsymbol{n}\cdot\boldsymbol{C}:\nabla\boldsymbol{v}$. In fact, since the prescribed boundary traction $\boldsymbol{t}^v$ is defined in terms of a constant stress tensor, the solution to (4.13) can be conveniently recast as

$$\boldsymbol{v}(\boldsymbol{\xi},\omega) = a\,\sigma^{\mathrm{F}}_{k\ell}(\boldsymbol{x}^0,\omega)\,\boldsymbol{\vartheta}^{kl}(\boldsymbol{\zeta}), \qquad \boldsymbol{\zeta}=(\boldsymbol{\xi}-\boldsymbol{x}^0)/a, \quad k,l=1,2,3, \tag{4.14}$$

in terms of the individual solutions $\boldsymbol{\vartheta}^{kl}=\boldsymbol{\vartheta}^{lk}$ to six canonical problems

$$\begin{aligned} \nabla_\zeta\cdot(\boldsymbol{C}:\nabla_\zeta\boldsymbol{\vartheta}^{kl}) &= \boldsymbol{0}, && \boldsymbol{\zeta}\in\mathbb{R}^3\setminus\overline{\mathcal{B}},\\ \boldsymbol{t}^{\vartheta} &= -\tfrac{1}{2}\,\boldsymbol{n}\cdot(\boldsymbol{e}_k\otimes\boldsymbol{e}_l+\boldsymbol{e}_l\otimes\boldsymbol{e}_k), && \boldsymbol{\zeta}\in\partial\mathcal{B}, \quad k,l=1,2,3, \end{aligned} \tag{4.15}$$

for the normalized cavity $\mathcal{B}$ in an infinite elastic solid where $\boldsymbol{t}^{\vartheta} = \boldsymbol{n}\cdot\boldsymbol{C}:\nabla_\zeta\boldsymbol{\vartheta}^{kl}$. It is useful to note that the reduced problems (4.15) are independent of $\boldsymbol{x}^0$ and a.

4.2 *Domain variation of the scattered field*

From (4.1), (4.5), (4.12) and (4.14), one finds that the limiting behaviour of (4.1) for vanishing cavity size can be synthesized as

$$\begin{aligned} \boldsymbol{u}^{\mathrm{S}}(\boldsymbol{x},\omega) = a^3|\mathcal{B}|\;\boldsymbol{e}_k\Big\{\hat{\boldsymbol{\sigma}}^k(\boldsymbol{x}^{\mathrm{O}},\boldsymbol{x},\omega):\boldsymbol{\mathcal{A}}:\boldsymbol{\sigma}^{\mathrm{F}}(\boldsymbol{x}^{\mathrm{O}},\omega) - \rho\,\omega^2\hat{\boldsymbol{u}}^k(\boldsymbol{x}^{\mathrm{O}},\boldsymbol{x},\omega)\cdot\boldsymbol{u}^{\mathrm{F}}(\boldsymbol{x}^{\mathrm{O}},\omega)\Big\}\\ + \boldsymbol{\varphi}(\boldsymbol{x}^{\mathrm{O}},\boldsymbol{x},\omega), \qquad \boldsymbol{x}\in\Omega\setminus\overline{B}_a, \quad |\boldsymbol{\varphi}|=o(a^3), \quad a\to 0, \end{aligned} \tag{4.16}$$

with the *constant* fourth-order tensor $\boldsymbol{\mathcal{A}}$ given by

$$\mathcal{A}_{ijkl} = \frac{1}{2\mu}\Big\{I_{ijkl} - \frac{\nu}{1+\nu}\delta_{ij}\delta_{kl}\Big\} - \frac{1}{|\mathcal{B}|}\int_{\partial\mathcal{B}}\vartheta_i^{kl}(\boldsymbol{\zeta})\,n_j(\boldsymbol{\zeta})\,\mathrm{d}\Gamma_\zeta. \tag{4.17}$$

4.3 *Infinitesimal cavity of spherical shape*

When vanishing spherical cavities are considered (that is, when $\mathcal{B}$ is a unit ball), the elastostatic exterior problem (4.13) can be recast in terms of spherical harmonics. In this way, an explicit solution to (4.13) can be obtained (see (**12**)) in the form

$$\begin{aligned} \boldsymbol{v}(\xi) = \frac{a^3}{4\mu}\Big[\frac{\boldsymbol{\sigma}^{\mathrm{F}}\boldsymbol{e}_r}{r^2} + \frac{r}{3}\,\boldsymbol{e}_r\times\nabla\times\left(\frac{\boldsymbol{\sigma}^{\mathrm{F}}\boldsymbol{e}_r}{r^2}\right) - \frac{4-10\nu}{7-5\nu}\,r\,\nabla\cdot\left(\frac{\boldsymbol{\sigma}^{\mathrm{F}}\boldsymbol{e}_r}{r^2}\right)\boldsymbol{e}_r\\ + \frac{5\nu-1}{3(7-5\nu)}\,r^2\nabla\nabla\cdot\left(\frac{\boldsymbol{\sigma}^{\mathrm{F}}\boldsymbol{e}_r}{r^2}\right) + \frac{r^2-a^2}{7-5\nu}\nabla\nabla\cdot\left(\frac{\boldsymbol{\sigma}^{\mathrm{F}}\boldsymbol{e}_r}{r^2}\right)\Big], \quad \boldsymbol{\xi}\in\mathbb{R}^3\setminus B_a, \end{aligned} \tag{4.18}$$

where $\boldsymbol{\sigma}^{\mathrm{F}} \equiv \boldsymbol{\sigma}^{\mathrm{F}}(\boldsymbol{x}^{\mathrm{O}},\omega)$ and $\boldsymbol{e}_r = \boldsymbol{e}_r(\boldsymbol{\xi})$ is the unit vector in the r-direction of the spherical coordinate system (r,θ,ϕ), originated at the centre of the cavity. On employing the identities

$$\begin{aligned}
\nabla\cdot\left(r^{-2}\boldsymbol{\sigma}^{\mathrm{F}}\cdot\boldsymbol{e}_r\right) &= r^{-3}\left[\operatorname{tr}\boldsymbol{\sigma}^{\mathrm{F}} - 3\,\boldsymbol{\sigma}^{\mathrm{F}}\!:(\boldsymbol{e}_r\otimes\boldsymbol{e}_r)\right],\\
\nabla\nabla\cdot\left(r^{-2}\boldsymbol{\sigma}^{\mathrm{F}}\cdot\boldsymbol{e}_r\right) &= -3r^{-4}\left[\{\operatorname{tr}\boldsymbol{\sigma}^{\mathrm{F}} - 5\,\boldsymbol{\sigma}^{\mathrm{F}}\!:(\boldsymbol{e}_r\otimes\boldsymbol{e}_r)\}\,\boldsymbol{e}_r + 2\,\boldsymbol{\sigma}^{\mathrm{F}}\cdot\boldsymbol{e}_r\right],\\
\boldsymbol{e}_r\times\left\{\nabla\times\left(r^{-2}\boldsymbol{\sigma}^{\mathrm{F}}\cdot\boldsymbol{e}_r\right)\right\} &= -3r^{-3}\left[\{\boldsymbol{\sigma}^{\mathrm{F}}\!:(\boldsymbol{e}_r\otimes\boldsymbol{e}_r)\}\,\boldsymbol{e}_r - \boldsymbol{\sigma}^{\mathrm{F}}\cdot\boldsymbol{e}_r\right],
\end{aligned} \tag{4.19}$$

and the fact that $r(\boldsymbol{\xi}) = a$ and $\boldsymbol{e}_r(\boldsymbol{\xi}) = -\boldsymbol{n}(\boldsymbol{\xi})$, $\boldsymbol{\xi}\in\Gamma_a$, for a spherical cavity, the boundary variation of $\boldsymbol{v}$ in (4.18), and thus that of $\boldsymbol{u}^{\mathrm{S}}$ as $a\to 0$ can be reduced to

$$\boldsymbol{v}(\boldsymbol{\xi}) = -\frac{a}{\mu}\Big[\frac{4-5\nu}{7-5\nu}\,\boldsymbol{\sigma}^{\mathrm{F}}(\boldsymbol{x}^{\mathrm{O}},\omega)\cdot\boldsymbol{n}(\boldsymbol{\xi}) - \frac{3-5\nu}{4(7-5\nu)}\,(\operatorname{tr}\boldsymbol{\sigma}^{\mathrm{F}}(\boldsymbol{x}^{\mathrm{O}},\omega))\,\boldsymbol{n}(\boldsymbol{\xi})\Big],\quad \boldsymbol{\xi}\in\Gamma_a. \tag{4.20}$$

By virtue of (4.20), the normalized solutions $\boldsymbol{\vartheta}^{kl}$ to (4.15) can be directly written as

$$\boldsymbol{\vartheta}^{kl}(\boldsymbol{\zeta}) = -\frac{1}{2\mu}\Big[\frac{4-5\nu}{7-5\nu}\Big\{n_l(\boldsymbol{\zeta})\,\boldsymbol{e}_k + n_k(\boldsymbol{\zeta})\,\boldsymbol{e}_l\Big\} - \frac{3-5\nu}{2(7-5\nu)}\delta_{kl}\,\boldsymbol{n}(\boldsymbol{\zeta})\Big],\quad \boldsymbol{\zeta}\in\partial\mathcal{B},$$

along the boundary of $\mathcal{B}$, where $\boldsymbol{n}(\boldsymbol{\zeta})$ is the normal outward to $\mathbb{R}^3\setminus\overline{\mathcal{B}}$. With such result and the identity

$$\int_{\partial\mathcal{B}}\boldsymbol{n}\otimes\boldsymbol{n}\;\mathrm{d}\Gamma_\zeta = \frac{4\pi}{3}\,\mathbf{I}_2,$$

which applies when $\partial\mathcal{B}$ is a unit sphere, the fourth-order tensor $\boldsymbol{\mathcal{A}}$ in (4.17) reduces to

$$\boldsymbol{\mathcal{A}} = \frac{3(1-\nu)}{2\mu(7-5\nu)}\left[5\,\mathbf{I}_4^{\mathrm{sym}} - \frac{1+5\nu}{2(1+\nu)}\,\mathbf{I}_2\otimes\mathbf{I}_2\right]. \tag{4.21}$$

On substituting (4.21) into (4.16), the limiting behaviour of (4.1) for a vanishing spherical cavity can be expressed explicitly as

$$\begin{aligned}
\boldsymbol{u}^{\mathrm{S}}(\boldsymbol{x},\omega) = \frac{4\pi a^3}{3}\,\boldsymbol{e}_k\Big[&\frac{3(1-\nu)}{2\mu(7-5\nu)}\Big\{5\,\hat{\boldsymbol{\sigma}}^k(\boldsymbol{x}^{\mathrm{O}},\boldsymbol{x},\omega)\!:\boldsymbol{\sigma}^{\mathrm{F}}(\boldsymbol{x}^{\mathrm{O}},\omega)\\
&- \frac{1+5\nu}{2(1+\nu)}\,(\operatorname{tr}\hat{\boldsymbol{\sigma}}^k(\boldsymbol{x}^{\mathrm{O}},\boldsymbol{x},\omega))\,(\operatorname{tr}\boldsymbol{\sigma}^{\mathrm{F}}(\boldsymbol{x}^{\mathrm{O}},\omega))\Big\} - \rho\,\omega^2\hat{\boldsymbol{u}}^k(\boldsymbol{x}^{\mathrm{O}},\boldsymbol{x},\omega)\cdot\boldsymbol{u}^{\mathrm{F}}(\boldsymbol{x}^{\mathrm{O}},\omega)\Big]\\
&+ \boldsymbol{\varphi}(\boldsymbol{x}^{\mathrm{O}},\boldsymbol{x},\omega),\qquad \boldsymbol{x}\in\Omega\setminus\overline{B}_a,\quad |\boldsymbol{\varphi}| = o(a^3),\quad a\to 0.
\end{aligned} \tag{4.22}$$

5. Topological derivative for elastic-wave imaging

From (2.1) and (2.7), one finds that the perturbation of the cost functional, $\mathcal{J}$, with respect to the creation of a hole in an otherwise intact (semi-infinite) medium can be written as

$$\begin{aligned}
&\mathcal{J}(\Omega\setminus\overline{B}_a;\boldsymbol{f}) - \mathcal{J}(\Omega;\boldsymbol{f})\\
&\quad= \frac{1}{2}\sum_{m=1}^{M}\Big[\{\overline{\boldsymbol{u}^{\mathrm{F}}+\boldsymbol{u}-\boldsymbol{u}^{\mathrm{obs}}}\}\cdot\boldsymbol{W}^m\cdot\{\boldsymbol{u}^{\mathrm{F}}+\boldsymbol{u}-\boldsymbol{u}^{\mathrm{obs}}\} - \{\overline{\boldsymbol{u}^{\mathrm{F}}-\boldsymbol{u}^{\mathrm{obs}}}\}\cdot\boldsymbol{W}^m\cdot\{\boldsymbol{u}^{\mathrm{F}}-\boldsymbol{u}^{\mathrm{obs}}\}\Big]\Big|_{\boldsymbol{x}=\boldsymbol{x}^m}\\
&\quad= \frac{1}{2}\sum_{m=1}^{M}\Big[\overline{\boldsymbol{u}}\cdot\boldsymbol{W}^m\cdot\boldsymbol{u} + 2\operatorname{Re}\Big(\{\overline{\boldsymbol{u}^{\mathrm{F}}-\boldsymbol{u}^{\mathrm{obs}}}\}\cdot\boldsymbol{W}^m\cdot\boldsymbol{u}\Big)\Big]\Big|_{\boldsymbol{x}=\boldsymbol{x}^m},
\end{aligned} \tag{5.1}$$

in terms of the scattered field $\boldsymbol{u}$. By virtue of (3.1), (4.16) and (5.1), the formula for topological derivative that is relevant to elastic wave imaging immediately follows as

$$\begin{aligned}\mathcal{T}(\boldsymbol{x}^{\mathrm{O}},\boldsymbol{f}) &= \lim_{a\to 0}\frac{1}{a^3|\mathcal{B}|}\sum_{m=1}^{M}\frac{1}{2}\Big[\overline{\boldsymbol{u}}\cdot\boldsymbol{W}^m\cdot\boldsymbol{u}+2\,\mathrm{Re}\Big(\{\overline{\boldsymbol{u}^{\mathrm{F}}-\boldsymbol{u}^{\mathrm{obs}}}\}\cdot\boldsymbol{W}^m\cdot\boldsymbol{u}\Big)\Big]\Big|_{\boldsymbol{x}=\boldsymbol{x}^m}\\ &= \sum_{m=1}^{M}\mathrm{Re}\Big[\{\overline{\boldsymbol{u}^{\mathrm{F}}(\boldsymbol{x}^m,\omega)-\boldsymbol{u}^{\mathrm{obs}}(\boldsymbol{x}^m,\omega)}\}\cdot\boldsymbol{W}^m\cdot\boldsymbol{e}_k\\ &\quad\times\Big(\hat{\boldsymbol{\sigma}}^k(\boldsymbol{x}^{\mathrm{O}},\boldsymbol{x},\omega):\boldsymbol{\mathcal{A}}:\boldsymbol{\sigma}^{\mathrm{F}}(\boldsymbol{x}^{\mathrm{O}},\omega)-\rho\,\omega^2\hat{\boldsymbol{u}}^k(\boldsymbol{x}^{\mathrm{O}},\boldsymbol{x},\omega)\cdot\boldsymbol{u}^{\mathrm{F}}(\boldsymbol{x}^{\mathrm{O}},\omega)\Big)\Big],\end{aligned}\tag{5.2}$$

with the Einstein summation convention assumed over index $k=1,2,3$. In particular, when B_a is a spherical cavity of radius a, expression (5.2) holds with the constant tensor $\boldsymbol{\mathcal{A}}$ given by (4.21), and the topological derivative takes the explicit form

$$\begin{aligned}\mathcal{T}(\boldsymbol{x}^{\mathrm{O}},\boldsymbol{f}) = \sum_{m=1}^{M}\mathrm{Re}\Big[\{\overline{\boldsymbol{u}^{\mathrm{F}}(\boldsymbol{x}^m,\omega)-\boldsymbol{u}^{\mathrm{obs}}(\boldsymbol{x}^m,\omega)}\}\cdot\boldsymbol{W}^m\cdot\boldsymbol{e}_k\Big(\frac{3(1-\nu)}{2\mu(7-5\nu)}\Big\{5\,\hat{\boldsymbol{\sigma}}^k(\boldsymbol{x}^{\mathrm{O}},\boldsymbol{x}^m,\omega):\boldsymbol{\sigma}^{\mathrm{F}}(\boldsymbol{x}^{\mathrm{O}},\omega)\\ -\frac{1+5\nu}{2(1+\nu)}\,(\mathrm{tr}\,\hat{\boldsymbol{\sigma}}^k(\boldsymbol{x}^{\mathrm{O}},\boldsymbol{x}^m,\omega))\,(\mathrm{tr}\,\boldsymbol{\sigma}^{\mathrm{F}}(\boldsymbol{x}^{\mathrm{O}},\omega))\Big\}-\rho\,\omega^2\hat{\boldsymbol{u}}^k(\boldsymbol{x}^{\mathrm{O}},\boldsymbol{x}^m,\omega)\cdot\boldsymbol{u}^{\mathrm{F}}(\boldsymbol{x}^{\mathrm{O}},\omega)\Big)\Big].\end{aligned}\tag{5.3}$$

It is worthwhile noting that on setting $\omega=0$ and replacing $\hat{\boldsymbol{u}}^k$ and $\hat{\boldsymbol{\sigma}}^k$ $(k=1,2,3)$ with their elastostatic counterpart, (5.3) can be shown to be in agreement with the results obtained in (**8**) for the three-dimensional elastostatic case.

For testing configurations synthesized in Fig. 1 where the incident seismic field is generated by a point force $\boldsymbol{f}$ acting at $\boldsymbol{x}^{\mathrm{S}}$ on the surface of the half-space, (5.3) can be further specialized by writing

$$\boldsymbol{u}^{\mathrm{F}}(\boldsymbol{x},\omega)=f_j\,\hat{\boldsymbol{u}}^j(\boldsymbol{x},\boldsymbol{x}^{\mathrm{S}},\omega),\qquad \boldsymbol{x}\in\Omega\backslash\bar{B}_a,\tag{5.4}$$

so that

$$\begin{aligned}\mathcal{T}(\boldsymbol{x}^{\mathrm{O}},\boldsymbol{f}) = f_l\sum_{m=1}^{M}\mathrm{Re}\Big[\{\overline{f_j\hat{\boldsymbol{u}}^j(\boldsymbol{x}^m,\boldsymbol{x}^{\mathrm{S}},\omega)-\boldsymbol{u}^{\mathrm{obs}}(\boldsymbol{x}^m,\omega)}\}\cdot\boldsymbol{W}^m\cdot\boldsymbol{e}_k\\ \times\Big(\frac{3(1-\nu)}{2\mu(7-5\nu)}\Big\{5\,\hat{\boldsymbol{\sigma}}^k(\boldsymbol{x}^{\mathrm{O}},\boldsymbol{x}^m,\omega):\hat{\boldsymbol{\sigma}}^l(\boldsymbol{x}^{\mathrm{O}},\boldsymbol{x}^{\mathrm{S}},\omega)\\ -\frac{1+5\nu}{2(1+\nu)}\,(\mathrm{tr}\,\hat{\boldsymbol{\sigma}}^k(\boldsymbol{x}^{\mathrm{O}},\boldsymbol{x}^m,\omega))\,(\mathrm{tr}\,\hat{\boldsymbol{\sigma}}^l(\boldsymbol{x}^{\mathrm{O}},\boldsymbol{x}^{\mathrm{S}},\omega))\Big\}\\ -\rho\omega^2\hat{\boldsymbol{u}}^k(\boldsymbol{x}^{\mathrm{O}},\boldsymbol{x}^m,\omega)\cdot\hat{\boldsymbol{u}}^l(\boldsymbol{x}^{\mathrm{O}},\boldsymbol{x}^{\mathrm{S}},\omega)\Big)\Big]\end{aligned}\tag{5.5}$$

with the summation convention assumed over indexes $j,k,l=1,2,3$. Similar to the restriction made in (4.5), here it is assumed that no two of the source point $\boldsymbol{x}^{\mathrm{S}}$, the observation point $\boldsymbol{x}^m$, and the trial point $\boldsymbol{x}^{\mathrm{O}}$ are coincident, a hypothesis that is common for this class of imaging problems.

A generalization of (2.1) and (5.2) through (5.5) to multiple seismic sources $\boldsymbol{f}^q$ ($q = 1, 2, \ldots Q$) is straightforward and involves external summation in the form of

$$\mathcal{J}_f(\cdot) \equiv \sum_{q=1}^{Q} \mathcal{J}(\cdot; \boldsymbol{f}^q) \quad \text{and} \quad \mathcal{T}_f(\cdot) \equiv \sum_{q=1}^{Q} \mathcal{T}(\cdot; \boldsymbol{f}^q). \tag{5.6}$$

A noteworthy feature of (5.5) and $(5.6)_2$ is that they are explicit in terms of the elastodynamic fundamental solution, which makes their computation relatively economical. Moreover, (5.5) and the approach leading to it in fact hold for any geometrical configuration Ω for which the elastodynamic fundamental solutions $\hat{\boldsymbol{u}}^\eta$ and $\hat{\boldsymbol{\sigma}}^\eta$ ($\eta = 1, 2, 3$) satisfying suitable boundary conditions on $\partial\Omega$ are known. This of course includes the infinite domain $\Omega = \mathbb{R}^3$ and the corresponding full-space fundamental solution.

6. Computational issues and results

For a testing configuration involving Q source points $\boldsymbol{x}^{\text{S}}$, M observation points $\boldsymbol{x}^m$, and a probing grid of N sampling points $\boldsymbol{x}^{\text{O}}$, computation of (5.5) involves $MQ + MN + NQ$ evaluations of the fundamental solution, thus permitting a computationally efficient exploration of the semi-infinite solid Ω for cavities. On evaluating $\mathcal{T}_f(\boldsymbol{x}^{\text{O}})$ over a suitable spatial grid spanning the volume of interest, regions in Ω where $\mathcal{T}_f$ takes the largest negative values constitute possible cavity locations (see (**7**) within the framework of shape optimization) and may be used to form an initial guess, in terms of the expected topology, location and shape of the hidden cavity, for a more refined gradient-based minimization. With reference to (5.3) and (5.5), it is also worth noting that $\mathcal{T} \equiv 0$ when $\boldsymbol{u}^{\text{F}} = \boldsymbol{u}^{\text{obs}}$, which infers no preferential cavity location.

In the context of shape optimization, an iterative algorithm based *entirely* on the topological derivative is also proposed (**8**) where for each iteration, holes are created in the solid wherever values of $\mathcal{T}$ fall below a certain (negative) threshold value. In the subsequent iteration, the total field in the cavitated solid serves as an unperturbed, 'free' field. In the present context of elastodynamics, however, evaluation of the equivalent of (5.5) for a cavitated half-space is in principle feasible but requires a computational effort that is several orders of magnitude larger than that associated with (5.5). For this reason, the stand-alone iterative minimization using exclusively topological derivatives is considered to be inferior to the proposed '*hybrid*' method which combines the grid search with gradient-based optimization. In what follows, the usefulness of the topological gradient given by (5.5) and (5.6b) in selecting an initial guess for the optimization-based approach to inverse scattering problems in elastodynamics will be demonstrated through numerical examples. First, the correctness of (5.5) is checked numerically in Section 6.1; with such result, the preliminary imaging of a single spherical cavity and a dual cavity system are presented in Sections 6.2 and 6.3, respectively.

6.1 *Comparison with BIE approximation*

In what follows, a reference will be made to the testing configuration depicted in Fig. 2. The 'true' cavity $\Omega_{\text{C}}^{\text{true}}$ is spherical, of diameter $D = 0.4d$, and centred at $(d, 0, 3d)$ inside the half-space. In succession, the cavity is illuminated by sixteen point sources $\boldsymbol{f}^q$ ($q =$

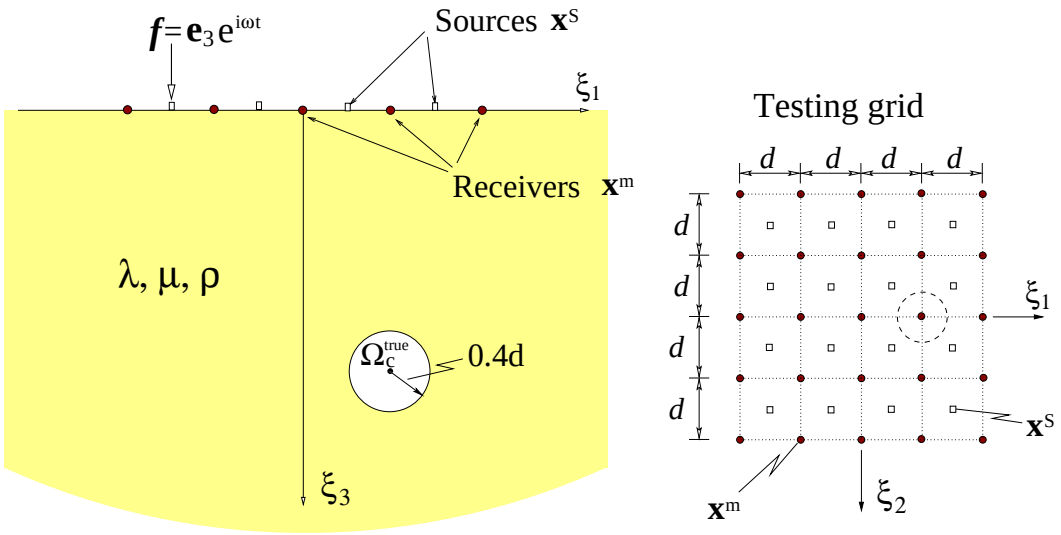

Fig. 2 Sample imaging problem

$1, 2, \dots 16$) acting normally on the surface of the semi-infinite solid; for each source location $\boldsymbol{x}^{\mathrm{S}}$, Cartesian components of the ground motion, $\boldsymbol{u}^{\mathrm{obs}}$, are monitored via twenty five sensors $\boldsymbol{x}^m$ distributed over the square testing grid. In the absence of physical measurements, experimental observations ($\boldsymbol{u}^{\mathrm{obs}}$) are simulated using the regularized BIE method (**10**) with the surface of the cavity discretized via eight-node quadratic boundary elements (**13**). To provide a focus for the numerical study, all topological gradients computed in the sequel are based on the formula (5.5) which postulates that the infinitesimal cavity is of *spherical* shape.

For simplicity, the matrices of weighting coefficients, $\boldsymbol{W}^m$ ($m = 1, 2, \dots M$) are taken as identity operators. In a general imaging situation involving repeated experiments with random measurement errors, $\boldsymbol{W}^m$ could be taken as an inverse of the data covariance operator characterizing $\boldsymbol{u}^{\mathrm{obs}}(\boldsymbol{x}^m)$ to discriminate between the waveform measurements with strong and poor signal-to-noise ratios (**14**).

To validate (5.5) numerically, a use is made of (5.1) so that the multi-source formula for $\mathcal{T}_f(\boldsymbol{x}^{\mathrm{O}})$ given by (5.6b) and (5.5) can be compared to its finite-difference approximation, $\tilde{\mathcal{T}}_f(\boldsymbol{x}^{\mathrm{O}}; a) = \sum_{q=1}^{Q} \tilde{\mathcal{T}}(\boldsymbol{x}^{\mathrm{O}}; \boldsymbol{f}^q, a)$, where

$$\tilde{\mathcal{T}}(\boldsymbol{x}^{\mathrm{O}}, \boldsymbol{f}; a) = \frac{3}{8\pi a^3} \sum_{m=1}^{M} \Big[\overline{\tilde{\boldsymbol{u}}^{\mathrm{S}}}(\boldsymbol{x}^m, \omega; \boldsymbol{x}^{\mathrm{O}}, a) \cdot \boldsymbol{W}^m \cdot \tilde{\boldsymbol{u}}^{\mathrm{S}}(\boldsymbol{x}^m, \omega; \boldsymbol{x}^{\mathrm{O}}, a) + 2\,\mathrm{Re}\big\{ \{ \overline{\boldsymbol{u}^{\mathrm{F}}(\boldsymbol{x}^m, \omega) - \boldsymbol{u}^{\mathrm{obs}}(\boldsymbol{x}^m, \omega)} \} \cdot \boldsymbol{W}^m \cdot \tilde{\boldsymbol{u}}^{\mathrm{S}}(\boldsymbol{x}^m, \omega; \boldsymbol{x}^{\mathrm{O}}, a) \big\} \Big] \Big|_{\boldsymbol{x}=\boldsymbol{x}^m} . \quad (6.1)$$

In (6.1), $\boldsymbol{u}^{\mathrm{F}}(\boldsymbol{x}^m, \omega) = f_j\, \hat{\boldsymbol{u}}^j(\boldsymbol{x}^m, \boldsymbol{x}^{\mathrm{S}}, \omega) = f_3\, \hat{\boldsymbol{u}}^3(\boldsymbol{x}^m, \boldsymbol{x}^{\mathrm{S}}, \omega)$ where $\boldsymbol{x}^{\mathrm{S}}$ is the point of action

Table 1 Number of surface elements in the BIE solution used for calculating $\boldsymbol{u}^{\rm obs}$ and $\tilde{\boldsymbol{u}}^{\rm S}$

$\bar{\omega}$	1.0	2.0	4.0	8.0
$\boldsymbol{u}^{\rm obs}$	216	216	384	384
$\tilde{\boldsymbol{u}}^{\rm S}\vert_{a=d/10}$	96			
$\tilde{\boldsymbol{u}}^{\rm S}\vert_{a=d/20}$	96	96		
$\tilde{\boldsymbol{u}}^{\rm S}\vert_{a=d/40}$	96	96	96	96
$\tilde{\boldsymbol{u}}^{\rm S}\vert_{a=d/80}$	96	96	96	96
$\tilde{\boldsymbol{u}}^{\rm S}\vert_{a=d/160}$		96	96	96
$\tilde{\boldsymbol{u}}^{\rm S}\vert_{a=d/320}$			96	96

of $\boldsymbol{f}$ and $\tilde{\boldsymbol{u}}^{\rm S}$ is, as an approximation to $\boldsymbol{u}$, computed via a BIE method by discretizing the surface of the trial spherical cavity Γ_a (with *fixed* small radius a) in terms of quadratic surface elements. As an illustration, a comparison between $\mathcal{T}_f$ and $\tilde{\mathcal{T}}_f$ is made at the interior point $\boldsymbol{x}^{\rm O}=(-d,d,2d)$ and four excitation frequencies

$$\bar{\omega} \equiv \omega d/c_s = k, \qquad c_s = \sqrt{\mu/\rho}, \qquad k = 1,2,4,8, \tag{6.2}$$

where c_s denotes the shear wave speed in the half-space. From (6.2), one may observe that the ratio between the shear wave length, λ_s, and the cavity diameter is approximately equal to $\lambda_s/D \approx 8/k$ ($k = 1,2,4,8$), thus characterizing the frequencies selected as those belonging to the so-called *resonance region* (**15**) where wave lengths are larger than or of a comparable size to the diameter of the scatterer. It is also worth noting that the resonance ('low-frequency') region is the one most commonly explored in the inverse acoustic and electromagnetic theory. For completeness, the number of boundary elements used for calculating $\boldsymbol{u}^{\rm obs}$ and $\tilde{\boldsymbol{u}}^{\rm S}$ in (5.5) and (6.1) at each excitation frequency is enclosed in Table 1.

In Fig. 3, the ratio $\tilde{\mathcal{T}}_f/\mathcal{T}_f$ is plotted versus the size of the trial cavity, a. From the display, one may observe that the finite difference results approach the respective 'exact' values given by (5.5) with diminishing a for all four frequencies. It is also worthwhile noting that the difference between $\tilde{\mathcal{T}}_f$ and $\mathcal{T}_f$ drops below 0.2% at the end of each curve. As might be expected, higher excitation frequencies (shorter wave lengths) require in general smaller values of a for an accurate finite difference estimate. The only exception to this rule is a 'faster' convergence of the results for $\bar{\omega} = 8$ than those for $\bar{\omega} = 4$; an anomaly apparently induced by the magnitude of $\mathcal{T}_f(\boldsymbol{x}^{\rm O},\omega)$ that is two decades larger at $\bar{\omega} = 8$.

6.2 *Preliminary imaging of a spherical cavity*

To examine the effectiveness of (5.5) as a tool for delineating plausible void locations in a semi-infinite solid, the imaging problem in Fig. 2 is taken as an example. For this testing configuration, the values of $\mathcal{T}_f(\boldsymbol{x}^{\rm O})$ are computed over the horizontal surface $S_h = \{\boldsymbol{\xi} \in \Omega | -5d < \xi_1 < 5d, -3d < \xi_2 < 3d, \xi_3 = 3d\}$ passing through the centroid of the 'true' cavity and plotted in Fig. 4 for the suite of frequencies (6.2). The computational grid is chosen so that the sampling points $\boldsymbol{x}^{\rm O}$ are spaced by $0.25d$ in both ξ_1 and ξ_2 directions. In

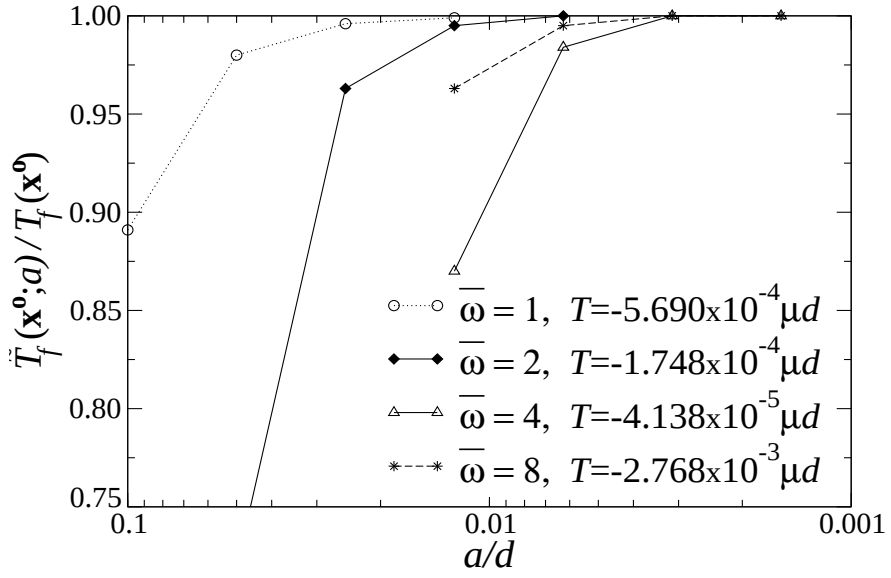

Fig. 3 Topological derivative estimates: finite difference versus explicit formula

the display, the red tones indicate negative values of $\mathcal{T}_f$ and thus possible cavity location; for comparison, the true cavity is outlined in white in each of the diagrams. The results indicate the potential of the topological derivative as an approximate, yet computationally efficient tool for exposing the cavity location, with 'higher' frequencies ($\bar{\omega} = 2, 4$) providing in general better resolution. From the diagram for $\bar{\omega} = 8$ where $\lambda_s/D \approx 1$, however, it is also evident that the topological derivative approach performs best when used in conjunction with wave lengths exceeding the cavity diameter. This is perhaps not surprising, since the assumption of an *infinitesimal* cavity, implicit to (3.1) and (5.5), is better conformed with by finite cavities that are '*small*' relative to the probing wavelength.

For completeness, the variation of $\mathcal{T}_f(\boldsymbol{x}^\circ)$ across the vertical planar region $S_v = \{\boldsymbol{\xi} \in \Omega | -5d < \xi_1 < 5d,\ \xi_2 = 0,\ 0.25d < \xi_3 < 6d\}$ is given in Fig. 5. Similar to the earlier diagram, the sampling points $\boldsymbol{x}^\circ$ are spaced by $0.25d$ in the ξ_1 and ξ_3 directions. A diminished resolution relative to the previous result reflects the major limitation of the 'experimental' data set, that is, the fact that both source and receiver points are limited to a single planar surface. Following the classical trade-off between the resolution and variance common to this class of inverse problems (**16**), the contour plots for $\bar{\omega} = 2$ and 4 exhibit greater accuracy than that for $\bar{\omega} = 1$, but are also plagued with local minima that are absent in the former diagram. Consistent with the previous assertion, the non-informative distribution of $\mathcal{T}_f$ for $\bar{\omega} = 8$ indicates that the use of topological derivative in elastic-wave imaging is most effective at 'low' excitation frequencies, that is, those inside the resonance region.

With diagrams such as those in Figs. 4 and 5, an algorithm for identifying plausible cavity

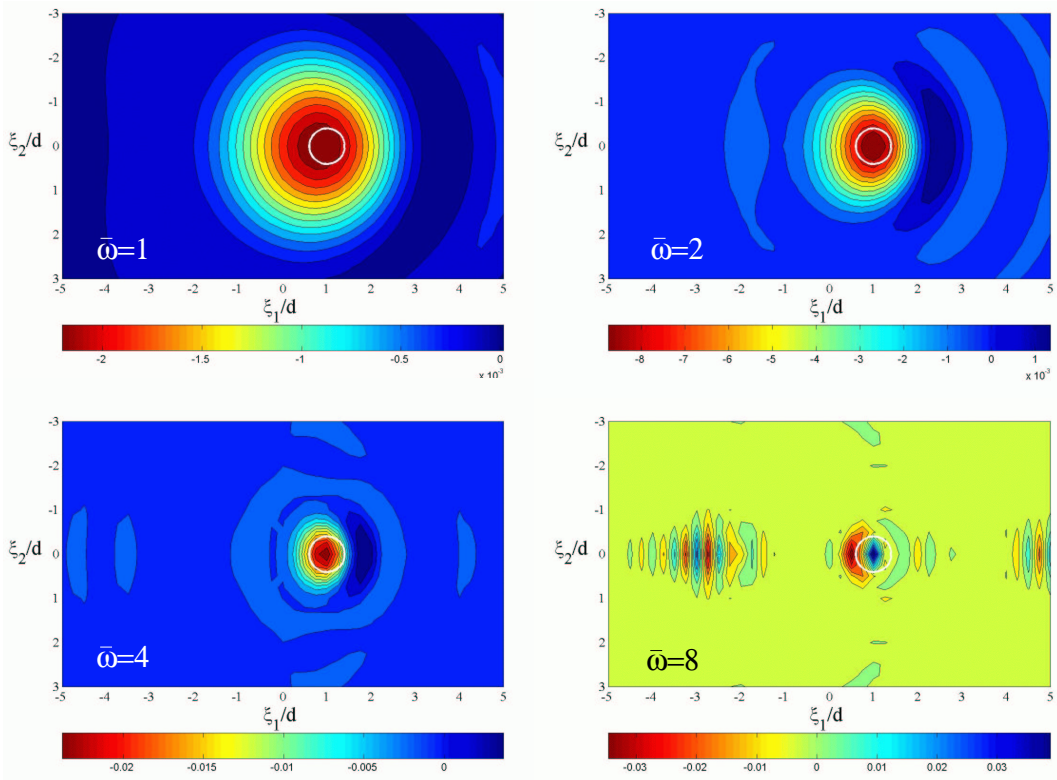

Fig. 4 Distribution of $(\mu d)^{-1}\mathcal{T}_f$ in the $\xi_3 = 3d$ (horizontal) plane: spherical cavity

locations could be devised on the basis of the non-zero distribution of an auxiliary function

$$\overset{\star}{\mathcal{T}}_f\,(\boldsymbol{x}^{\mathrm{O}}) = \begin{cases} \mathcal{T}_f(\boldsymbol{x}^{\mathrm{O}}), & \mathcal{T}_f < C, \\ 0, & \mathcal{T}_f \geq C, \end{cases} \tag{6.3}$$

where $C < 0$ denotes a suitable threshold value. With such definition, it is also possible to combine the individual advantages of different probing wavelengths by employing the product of (6.3) at several frequencies. As an illustration of the latter approach, Fig. 6 plots the distribution of the product of $\overset{\star}{\mathcal{T}}_f\,|_{\bar{\omega}=1}$ and $\overset{\star}{\mathcal{T}}_f\,|_{\bar{\omega}=2}$ in the vertical plane, with C set to approximately 40% of the global minima of the respective distributions in Fig. 5. Despite the limited accuracy and multiple minima characterizing respectively the individual solutions for $\bar{\omega} = 1$ and $\bar{\omega} = 2$, the combined result stemming from (6.3) points to a single cavity with its centre and size closely approximating the true void configuration.

6.3 *Multiple void problem*

In view of the fundamental assumption underlying (5.5), that is, a single spherical hole (of infinitesimal radius) is created inside the semi-infinite solid, it is important to evaluate the

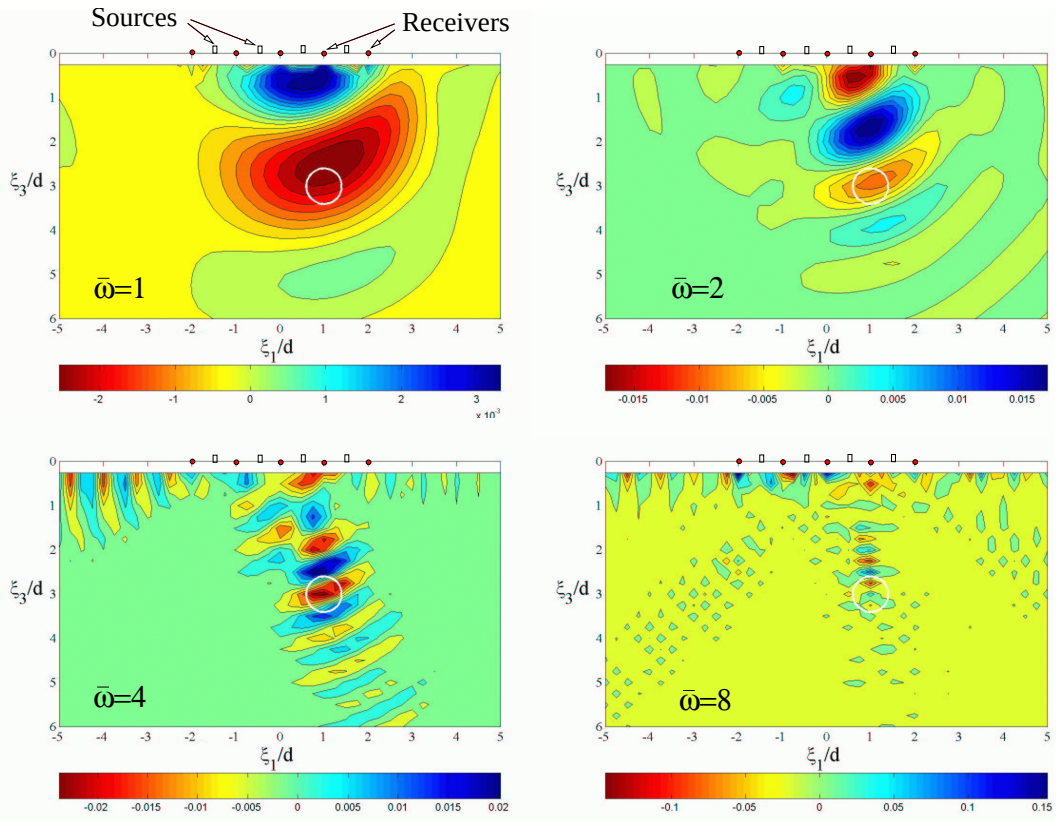

Fig. 5 Distribution of $(\mu d)^{-1}\mathcal{T}_f$ in the $\xi_2 = 0$ (vertical) plane: spherical cavity

performance of the topological derivative approach in situations involving non-spherical or multiple cavities. To this end, consider the constellation given in Fig. 7 where the hidden cavity system ($\Omega_{\mathrm{C}}^{\mathrm{true}}$) consists of a spherical void of radius $D = 0.4d$ and an ellipsoidal void whose principal semi-axes, $(D_1, D_2, D_3) = (0.4d, 1.2d, 0.6d)$, are aligned with the reference Cartesian frame. The two cavities are centred respectively at $(-d, d, 2d)$ and $(2d, d, 2d)$ inside the half-space. Also indicated in the Figure is the boundary element mesh used to simulate the experimental measurements. For comparison with the previous example, the surface testing configuration is assumed to be the same as that in Fig. 2.

Fig. 8 plots the distribution of $\mathcal{T}_f(\boldsymbol{x}^{\mathrm{o}})$ across $\xi_3 = 2d$ and $\xi_2 = d$ planes for two representative frequencies, $\bar{\omega} = 1$ and $\bar{\omega} = 2$. As a reference, intersection of the 'true' cavity system with the respective cutting planes is outlined in white in each of the graphs. In the top left diagram, the pear-shaped lower frequency contours ($\bar{\omega} = 1$) for the horizontal plane correctly envelop both cavities, albeit failing to provide a more detailed map of the void system. In contrast, the distribution of $\mathcal{T}_f|_{\xi_3=2d}$ for $\bar{\omega} = 2$ not only points to the correct number of cavities, but also reasonably approximates their individual shapes. Similar to

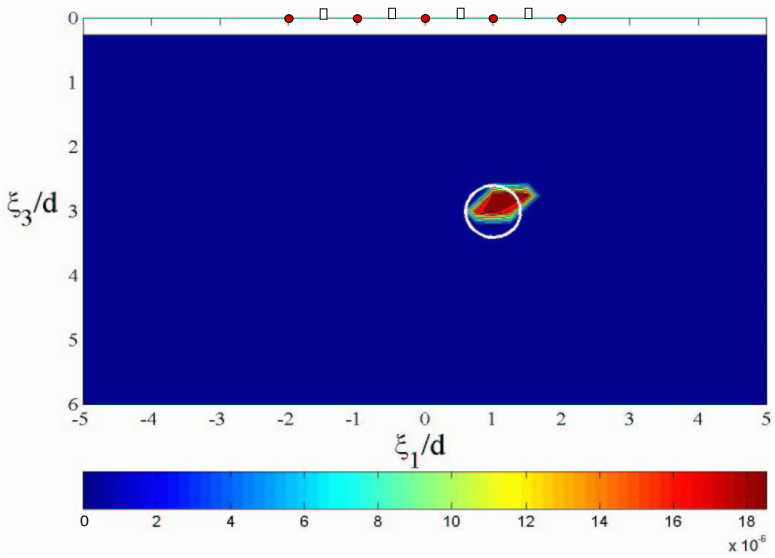

Fig. 6 Distribution of $(\mu d)^{-2}\, \overset{\star}{T}_f|_{\bar{\omega}=1} \times \overset{\star}{T}_f|_{\bar{\omega}=2}$ in the $\xi_2 = 0$ plane: spherical cavity

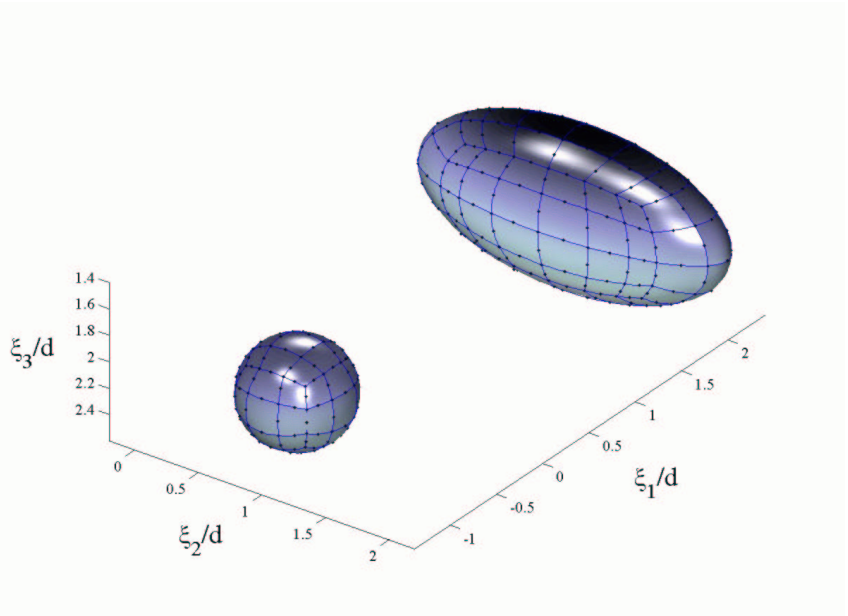

Fig. 7 Geometry and discretization of the multiple void domain in the half-space ($\xi_3 > 0$)

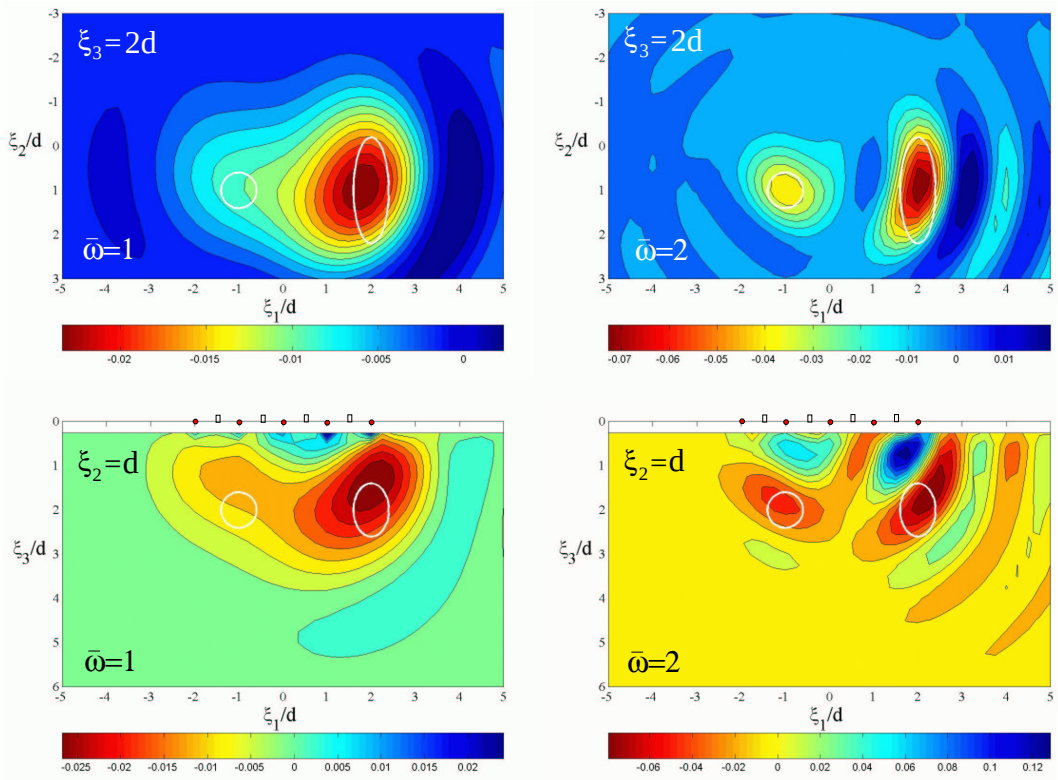

Fig. 8 Distribution of $(\mu d)^{-1}\mathcal{T}_f$ in the $\xi_3 = 2d$ and $\xi_2 = d$ planes: dual cavity problem

the previous example, the results for the vertical ($\xi_2 = d$) plane are characterized by a somewhat diminished resolution, caused primarily by the limited aperture of the testing grid. In view of the latter limitation, the proposed imaging tool is expected to work best with relatively simple, smooth cavity shapes.

Following the multi-frequency approach outlined earlier, Fig. 9 plots the distribution of the product between $\overset{\star}{\mathcal{T}}_f|_{\bar{\omega}=1}$ and $\overset{\star}{\mathcal{T}}_f|_{\bar{\omega}=2}$ as a means to enhance the imaging resolution in the vertical plane $\xi_2 = d$. With reference to (6.3), the threshold values of C used to calculate $\overset{\star}{\mathcal{T}}_f$ at each frequency are set to approximately 30% of the global minima of the respective ($\xi_3 = 2d$) distributions in Fig. 8. Notwithstanding the evident lack of accuracy relative to the images in the horizontal plane, the hybrid contour image in Fig. 9 unequivocally points to two distinct cavities approximating the true void constellation.

6.4 *Additional considerations*

The foregoing examples illustrate the potential of topological derivative as a robust, albeit approximate tool for exposing cavities hidden in a semi-infinite solid from elastic

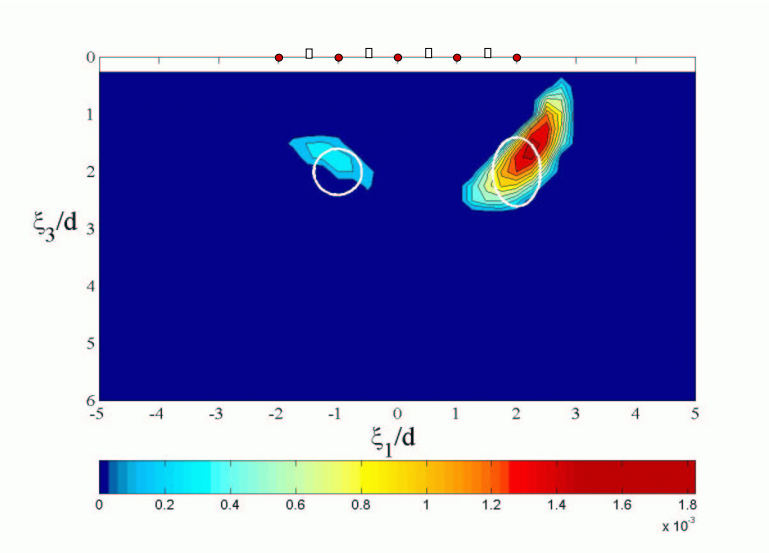

Fig. 9 Distribution of $(\mu d)^{-2}\, \overset{\star}{\mathcal{T}}_f|_{\bar{\omega}=1} \times \overset{\star}{\mathcal{T}}_f|_{\bar{\omega}=2}$ in the $\xi_2 = d$ plane: dual cavity problem

waveform measurements. With such features, the proposed methodology can be regarded as a full complement to the gradient-based BIE imaging algorithm (**4**), whose high resolution potentials are critically dependent on suitable parametrization, and thus on prior information describing the cavity location, topology, and geometry. To build a comprehensive computational platform for the three-dimensional inverse analysis of void-scattered elastic waves, a hybrid scheme could thus be devised where a computationally-effective probing tool such as (5.5) is used to explore the volume of interest in a grid-type fashion and thus furnish suitable prior information for the more refined, gradient-based imaging stage.

In situations where an approximate location of the void is unknown beforehand, a construction of its full three-dimensional image in the context of previous examples would entail an inspection of many cutting planes and thus an excessive number of sampling points. To mitigate the problem, an algorithm similar to that proposed for the linear sampling method in acoustics (**17**) could be adopted. In such iterative scheme, a volume of the host solid under consideration would be initially partitioned into a $2 \times 2 \times 2$ grid of cubes; the topological derivative $\mathcal{T}_f$ would then be evaluated at their centroids, and each cube where $\mathcal{T}_f$ falls below a certain threshold value would further be subdivided into eight $(2 \times 2 \times 2)$ sub-cubes for the next iteration.

7. Summary

In this communication, the concept of topological derivative that has its origins in elastostatics and shape optimization is extended to three-dimensional elastic-wave imaging of semi-infinite and infinite solids. On taking the limit of the boundary integral

representation of the scattered field caused by a spherical cavity with diminishing radius, the topological derivative, which quantifies the sensitivity of the featured cost functional due to the creation of an infinitesimal hole, is formulated explicitly in terms of the elastodynamic fundamental solution. A set of numerical examples involving a planar testing surface on top of the semi-infinite solid is included to validate and illustrate the proposed imaging algorithm wherein plausible void regions are delineated through negative values of the topological derivative at sampling points. The results for both single and multiple cavity configurations indicate that the approach is most effective when used at frequencies inside the resonance region, that is, with wave lengths exceeding the cavity diameter. It is also found that the use of multiple excitation frequencies as a tool to illuminate the cavity may enrich the experimental data set and thus mitigate the geometric limitations of the assumed planar testing surface. To the authors' knowledge, an application of topological derivative to inverse scattering problems has not been attempted before; the approach proposed in this study can be extended to deal with acoustic problems as well.

Acknowledgment

The support provided by the National Science Foundation through CAREER Award No. CMS-9875495 to B. Guzina and the University of Minnesota Supercomputing Institute during the course of this investigation is kindly acknowledged. Special thanks are extended to MTS Systems Corporation for providing the opportunity for M. Bonnet to visit the University of Minnesota through the MTS Visiting Professorship of Geomechanics.

References

1. R. E. Sheriff and L. P. Geldart. *Exploration Seismology* (Cambridge University Press, 1995).
2. R. E. Plessix, Y. H. De Roeck and G. Chavent. *SIAM J. Sci. Comput.* **20** (1999) 1033–1052.
3. D. Colton and R. Kress. *Integral Equation Method in Scattering Theory* (Wiley, New York, 1983).
4. B. B. Guzina, S. Nincheu Fata and M. Bonnet. *Int. J. Solids Struct.* **40** (2003) 1505–1523.
5. H. A. Eschenauer, V. V. Kobelev and A. Schumacher. *Structural Optimization* **8** (1994) 42–51.
6. A. Schumacher. *Topologieoptimierung von Bauteilstrukturen unter Verwendung von Kopchpositionierungkrieterien*. Ph.D. thesis, Univ. of Siegen, Germany (1995).
7. J. Sokolowski and A. Zochowski. *SIAM J. Control Optim.* **37** (1999) 1251–1272.
8. S. Garreau, P. Guillaume and M. Masmoudi. *SIAM J. Control Optim.* **39** (2001) 1756–1778.
9. R. Gallego and G. Rus. *Proc. IABEM 2002 Conference,* Austin, Texas, CD-ROM (2002).
10. R. Y. S. Pak and B. B. Guzina. *Int. J. Solids Struct.* **36** (1999) 4743–4766.
11. B. B. Guzina and R. Y. S. Pak. *Int. J. Solids Struct.* **36** (1999) 493–516.
12. A. I. Lurie. *Theory of Elasticity* (Izdatelstvo Nauka, Moscow (in Russian), 1970).
13. C. A. Brebbia, J. C. F. Telles and L. C. Wrobel. *Boundary Element Techniques* (Springer Verlag, 1984).

14. A. Tarantola. *Inverse Problem Theory* (Elsevier, Amsterdam, 1987).
15. D. Colton and R. Kress. *Inverse Acoustic and Electromagnetic Scattering Theory* (Springer Verlag, 1992).
16. W. Menke. *Geophysical Data Analysis: Discrete Inverse Theory* (Academic Press, San Diego, 1989).
17. D. Colton, K. Giebermann and P. Monk. *SIAM J. Sci. Comput.* **21** (2000) 2316–2330.